Algal Research 91 (2025) 104331

Contents lists available at ScienceDirect

Algal Research

journal homepage: www.elsevier.com/locate/algal

Impact of bubbles on the light field within a photobioreactor: A practical design tool

Victor Pozzobon

Université Paris-Saclay, CentraleSupélec, Laboratoire de Génie des Procédés et Matériaux, Centre Européen de Biotechnologie et de Bioéconomie (CEBB), 3 rue des Rouges Terres 51110 Pomacle, France

ARTICLE INFO

Keywords:
Microalgae
Light
Bubbles
Absorption
Scattering
Monte Carlo
Raytracing

ABSTRACT

Bubbles can be strong modulators of the light field they interact with. An example of such a configuration is a photobioreactor hosting a microalgae culture where bubbles and cells contributions entangle. To investigate this question, this work computed bubble distribution in a photobioreactor setup using OpenFOAM. Then, Ray Tracing coupled with the Monte Carlo Method was used to calculate the light over 3240 configurations (cell concentrations, strains, pigment profiles, void fraction, etc.). From a physical perspective, this investigation showed that the presence of bubbles lengthens the ray path within the culture medium and increases the apparent absorption. In addition, a sizable amount of the incident light can be reflected and scattered away (about 10% for a 2.15% void fraction). From a numerical perspective, using a dimensionless approach and physics-based formulation, the whole knowledge of the database was condensed into an exponential decay (Beer–Lambert like) model. The methodology was first used on a bubble-free setup (360 profiles), where it delivered accurate local and global predictions of the light and the reflected light fraction. Then, it was expanded to the whole database. All in all, it allowed to compute the local light field, total distributed energy, and reflected light fraction with accuracies (MARE) of 9.50, 2.25, and 6.35%, respectively. It also allowed to distinguish between bubbles and microalgae contributions. Owing to its simplicity and computational efficiency, the model can be used to precisely account for detailed light distribution in large-scale models, opening the way to improving the computation of country-scale microalgae cultivation performances.

1. Introduction

Since the middle of the last century, humanity has started to put tremendous stress on its ecosystem. Despite technological progress, pressure on fossil fuels, water, arable lands, and biodiversity is peaking, inducing deleterious environmental consequences [1]. In addition, the modern lifestyle (lack of physical activity and excessive consumption of transformed food products) causes adverse health effects, lumped under the term metabolic syndrome [2]. Facing this dire situation, mankind regards microalgae as part of the solution. Indeed microalgae photoautotrophic cultivation produces quality food/feed [3,4] and high-value bio-sourced molecules [5,6]. Besides, it comes with environmental benefits such as carbon dioxide cycling, water pollutions remediation (nitrogen, phosphorous) [7,8], and possible valorization as biofuel of extraction processes leftovers [9]. Finally, it can be led on non-arable lands avoiding competition with current food-producing cultures.

Photoautotrophic microalgae cultures are led in specific vessels called photobioreactors. The specificity of this type of biochemical reactor is to inherently host three phases: liquid - the culture medium -, solid - the microalgal cells -, and gas - often air (possibly enriched in carbon dioxide). The later is crucial as is supplies inorganic carbon, removes photogenic oxygen, and ensures mixing -. On top of this complexity comes light, as a photobioreactor has to ensure adequate contact between the cell and the actinic illumination. Due to this complexity, the question of photobioreactor optimal design is still very open today. On one side of the spectrum lie open ponds, which are inexpensive and easily scalable but challenging to operate owing to their high hydraulic retention time and contamination-prone nature [10]. On the other side, lie closed vessels, which are often expensive owing to their complex design and wealthy instrumentation [11]. In addition to these two well-known categories, the systems can also be distinguished by their orientation, i.e., horizontal, such as raceway ponds [10] and tubular photobioreactor [12], or vertical, ranging from bubble columns [13] to building façade-integrated flat panel photobioreactors [14].

For both types of systems, scholars and engineers are constantly working to improve the design and operation. In this matter, Computational Fluid Dynamics (CFD) is often used. Indeed, this mathematical method allows from testing ideas in an inexpensive manner to in-depth fine-tuning of a promising design. Raceway ponds are the systems

E-mail address: victor.pozzobon@centralesupelec.fr.

https://doi.org/10.1016/j.algal.2025.104331
Received 29 April 2025; Received in revised form 21 September 2025; Accepted 22 September 2025
Available online 29 September 2025

Nomenclature

Latin symbols	Property	Unit
Bo	Bond number	–
C	Microalgae concentration	kg/m^3
D	Sparging orifice diameter	m
d	Bubble diameter	m
Fr	Froude number	–
g	Gravity acceleration	m/s^2
g	Henyey-Greenstein phase function parameter – Asymmetry coefficient	–
I	Light intensity	$\mu molPhoton/m^2/s$
J	Spectral radiance	$W/m^2/nm/sr$
L	Distance	m
m	Relative refraction index	–
n	Refraction index	–
p	Phase shift parameter	–
R	Reflectivity	–
$\vec{s}$	Direction vector	–
u	Velocity	m/s
w	z component of the velocity vector	m/s
$\vec{x}$	Position	m
z	Running depth	m

Greek symbols	Property	Unit
α	Void fraction	–
β	Fitting parameter	–
Γ	Surface tension	N/m
γ	Fitting parameter	–
ζ	Fitting parameter	–
θ	Angle	rad
λ	Wavelength	nm
ξ	Size parameter	–
ρ	Reflected fraction of incident light	–
ϱ	Density	kg/m^3
σ	Cross section	m^2/kg
Φ	Phase function	–
ϕ	Fitting parameter	–
Ω	Angle (for integration)	rad
ω	Fitting parameter	–

Subscript	Description
A	Absorption
b	Bubble
D	Depth
e	Event
H	Height
i	Incident or intersection (in the flow chart diagram)
l	Liquid
r	Refraction
S	Scattering
W	Width
0	Incident (for light intensity)

that benefited the most from fluid-only CFD investigation (*e.g.*, to reduce medium circulation power consumption [15]). However, studies focusing only on fluid flow are rare. Indeed, the fluid flow is often coupled with a light field to dissect microalgae/interaction in terms of light/dark cycle. For example, tubular photobioreactors have been coupled numerically with a static mixer to induce a controlled light/dark cycle. The first studies approximated light by the cell radial position and delivered a one-mixer system as proof of concept [16]. Nowadays, this approach has been refined by exploring the effect of the number of units and accounting for realistic light fields [17,18]. Raceway ponds have also been explored, and the importance of the paddlewheel was underlined, as the microalgae do not move between fluid layers when circulating [19].

Still, while horizontal production systems have drawn some attention to the matter, vertical systems have garnered the most interest. Indeed, their vertical nature offers an additional means to fine-tune the light/dark cycle: bubble circulation. The gas phase offers another lever to direct microalgae/light interaction. For example, in the simplest design possible, the bubble column, increasing the superficial gas velocity increases the light/dark cycle frequency [13]. Then comes a refinement of the bubble column: the airlift concept (featuring a riser and a downcomer section), where manipulating the gas void fraction allows it to act on the light and dark phase durations (the longer

the cycle time, the worse the performances) [20]. Still, as those long light/dark alternations seemed to hinder productivity, authors came up with the idea of a baffle airlift photobioreactor [21,22], where small lateral deflectors create local recirculations incidentally speeding up the light/dark alternations. In addition, to take advantage of bubble-induced circulation, this concept offers many geometrical parameters (baffle position, geometry, inclination, frequency, etc.) to act on in order to stir the process towards the desired output [23]. Finally, bubbles allow for even more exotic designs, such as Taylor vortex [24] or annular [25] photobioreactors.

In the case of numerical modeling, accurately computing the light field is key in order to properly capture the phenomena of interest (from the photoinhibition zone in the periphery of the reactor to the aphotic zone at its core or the light/dark cycles perceived by the cells). In this respect, several techniques have been used. The most convenient method might be using Beer–Lambert models [26,27], sometimes refined to account for cylindrical geometries [28,29], or simply uncorrected by the geometry [25]. This approach incidentally neglects scattering, which lowers the quality of the predictions. To alleviate the problem, Cornet has proposed to apply Schuster's model 1D two-flux model (feature strong assumption, such as 50% backscatter, and not accounting for oblique rays) to apprehend this problem better [30,31] and expanded it to cylindrical and spherical geometries [32]. This model became quite popular, especially when dealing with 1D planar systems such as microalgae biofaçade flat panel module [33], raceway ponds [34], or spectrophotometer cuvette [35]. Then come methods for solving the Radiative Transport Equation (RTE) with higher accuracy. Among them, one can note the Discrete Ordinates Method [13,36], or the Ray Tracing method, classically coupled with Monte Carlo sampling (a.k.a. MCMRT) [37]. In any case, these models require incremental knowledge of the biomass radiative characteristics, incremental computational power, and applied mathematics skills, with a notable exception for MCMRT.

Taking a step back, while authors used quite complex models featuring bubbly flow, microalgae motion, and light field, very few actually evaluated the questions of bubble effects on a light field. Some authors clearly stated that they neglected void fraction in solving the Radiative Transport Equation [13], but most did not even mention it. This lack of consideration can be a problem, given the pivotal role of light in the photosynthesis process. Furthermore, no author evoked the question of the light reflected and/or scattered away from the photobioreactor, which alters the overall energy balance. This state of fact can be explained by the lack of an easy-to-use tool to apprehend the questions at hand. This work aims to remediate this problem.

When investigating this question, several elements have to be taken into account. First of all, small bubbles (hundreds of microns to a few millimeters diameters) are best suited for photobioreactor in terms of mixing and gas transfer [38]. Second, depending on the flow regime, such bubbles can either be drawn towards the wall (wall peaking), towards the core of the flow (coring), or dispersed somewhat homogeneously (saddle profile) [39], which underlines the need to compute a physics-accurate bubble position distribution before computing the spatial variation of the light field. Third, the presence of bubbles (or any body with a refraction index different from the medium) induces additional scattering that modifies the local light field (see the pioneering work of van Hulst [40] for detailed and pedagogical explanations).

Only two studies explicitly address the phenomenon of interest in the context of microalgae cultivation. First is the work of Berberoglu [41], who investigated dihydrogen production by cyanobacterium *Anabaena variabilis*. As dihydrogen production is driven by photosynthesis, light field and microbubbles (25 to 150 μm in this case) cannot be separated at the process level. The authors assumed an ideal incident light profile and divided the visible spectrum into different bands (owning to the cyanobacterium radiative properties, modeled using the Henyey-Greenstein scattering phase function) before employing Mie theory to derive the light field within the reactor. Yet, they did not account for a potential spatial variability of the distribution of the bubbles within the culture volume. Second, comes the contribution of McHardy et al. [42] who spatially resolved the bubble distribution within a bubble column photobioreactor (Euler-Euler simulation, with quite large bubbles were assumed - 7 mm diameter -). Throughout their investigations, the authors showed that heterogeneous bubble concentration effectively retroacted the local light field. Still, in order to garner a holistic view, the scope of the literature survey has to be widened from photobioreactor-focused investigations to a more general setup that is near wall bubbles in a radiative field. For example, conclusions on the importance of bubbles on the local light field have also been underlined in the case of photocatalytic wastewater treatment in a bubble column [43]. Moving away from liquid containing setups, the case of bubbles trapped in manufactured glazing, which can be deemed similar, has been investigated by Pilon et al. [44,45]. The authors showed that in the case of infrared radiation, Mie, Far-field, and Near-field approaches yielded similar results as the matrix absorption was relatively high, underlining the importance of the relative radiative properties values (between the bubble and the medium). Finally, in an even more exotic setup, Dombrovskii investigated the radiative behavior of a failing nuclear core (surface temperature of 2000 to 3000 K) releasing heat by radiation into boiling water. Being one of the few to correctly apply van Hulst's guidelines, the author demonstrated that a fraction of the emitted power is actually sent back to the nuclear core because of the bubbles [46]. In the case of microalgae culture, this could translate into part of the incident of light being cast away from the culture by the bubbles. Furthermore, Dombrovskii underlined that geometrical optics could safely be used in this case (near-infrared illumination and bubble diameter above 8 μm) as opposed to anomalous diffraction.

Having acknowledged the need for investigation, this work aims to create new knowledge of the effect of bubbles on the local light field in the specific context of microalgae cultivation. To do so, bubble distribution will be derived in a physics-accurate manner using CFD. Then, MCMRT will be used to derive the local light field and reflected (and scattered) light over a wide range of operating conditions (microalgae concentration, microalgae pigmentation, bubble size, and void fraction). In order to increase the generality of the results, a dimensionless approach (within relevant ranges) will be undertaken to provide an easy-to-use model for scholars and engineers to apply to their use cases.

2. System

The system considered here is a fluid volume belonging to a large photobioreactor. This fluid zone has a cubic shape. The fluid domain hosts a dispersed bubble phase and microalgae suspended within a culture medium. The culture is considered as a continuum, with radiative properties varying as a function of the cell concentration. As parts of an infinite domain, the described region is surrounded by paired cyclic boundary conditions. The gravity is oriented downward, leading to an upward bubble motion. From a radiative perspective (Fig. 1 - Right), collimated light is assumed from one lateral face of the cubic domain. Internally, light rays can be absorbed or scattered by microalgae, as well as reflected or diffracted by the bubbles. When crossing the illuminated face again, the rays are considered lost.

3. Liquid and gas phase models

While the previous section introduced the system, the following one covers the physical assumptions, their validity ranges, and the numerical details of the calculation realization. The chosen approach belongs to the Euler–Lagrange family. The rationale behind the choice of an Euler–Lagrange model is quite simple. Among the different methods able to predict gas–liquid flows, interface-resolving methods (*e.g.*, Volume of fluid [47]) would not allow to simulate a domain large

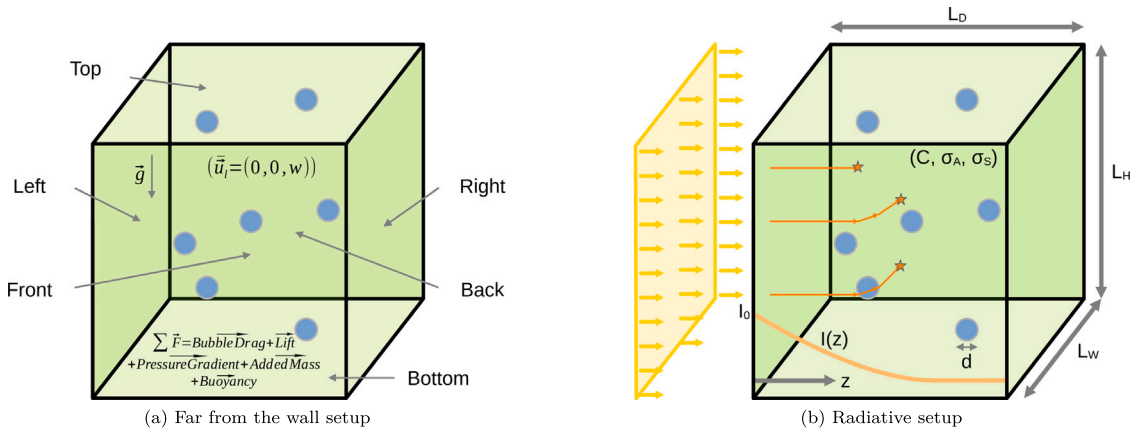

(a) Far from the wall setup (b) Radiative setup

Fig. 1. Considered setups. Left - Fluid flow setup. Right - Radiative setup (rays are cast from the left side boundary towards the inner domain). $L_D = L_H = L_W = 100d$. Boundaries paired together to create the cyclic setup: Top & Bottom, Left & Right, Front & Back.

enough, and Euler-Euler methods do not describe bubble positions *per se* [42]. Euler–Lagrange approaches are the only ones capable of simulating a large domain and precisely locating the bubbles within it, at the price of losing the precise shape of the interfaces.

3.1. Liquid phase model

The system is considered to host two phases: the growth medium, including the microalgae, considered together as a continuum, and the bubbles, considered as a dispersed gaseous phase. Euleriean approach is used for the continuum, while the dispersed phase is described as Lagrangian particles. Equations and numerical specificities have been published previously [29]; only the main features will be presented here. The liquid flow is modeled using classical incompressible Navier Stokes equations, considering the growth medium as a Newtonian fluid. While valid for low-concentration cultures (below a volume fraction of 0.70% for freshwater *Chlorella* sp.) [48], this assumption could be discussed for high-density ones. Fortunately, as it will be shown later, such values are not encountered here. Furthermore, bubbles contribute to the evolution of the continuous phase momentum (based on the reciprocal forces exerted by one another). Given the cyclic setup (Fig. 1 - Left), no sizable momentum sink exists. This may lead to non-physical behavior, such as very high liquid rising velocity (driven by the bubbles despite them keeping a reasonable sliding velocity). To avoid such an artifact, an artificial momentum sink (driving velocity downward at 0.2 m/s) was added. Finally, turbulence was not encountered as the maximum bubble Reynolds number was low (about 214). While it may seem surprising as Bubble Induced Turbulence (BIT) models exist, one has to remember that those models are intended to account for the complex bubble swarm wakes intertwining (referred to as pseudo-turbulence) in Euler-Euler simulations [49].

Liquid properties are taken as those of 20 °C water (density: 998 kg/m^3, viscosity: 1.0 10^{-3} Pa.s, air–water surface tension: 72 mN/m).

3.2. Gas phase model

Bubbles are described using a Lagrangian approach. The tracers are suggested to several forces: buoyancy, virtual mass, drag coefficient, pressure gradient, and lift. The description retained for the study assumes bubbles to be spherical, which restricts the upper range of bubble diameter to ensure an adequate description. Bubble sphericity can be assessed by the balance between the buoyancy force and the surface tension. It materializes into the Bond number (Eq. (1)):

$$Bo = \frac{(\varrho_l - \varrho_b) g d^2}{\Gamma} \tag{1}$$

where ϱ_b is the gas density (taken as 1.2 kg/m^3), ϱ_l is the continuum density, g is the gravity, and Γ is the surface tension.

Assuming a maximum Bond number of 1 leads to a maximum bubble diameter of 2.71 mm. This value is to be compared to the one of classical bubbles generated by industrial spargers made of sintered steel (rod shape). For this calculation, several assumptions have to be drawn. First, the data based on the manufacturer's datasheet (available on the Internet) is considered exact. In this case, the following characteristics can be considered: 15 to 45% porosity, pore diameter from 1 to 60 μm, length 40 inches, and diameter 2 inches. In order to be conservative, only the largest pores are considered to generate bubbles (*i.e.*, 60 μm), and the porosity is taken in the middle of the range (30%). Then, taking the case of a 2-meter high, 1-meter long, 10-centimeter deep photobioreactor aerated at 0.1 vvm (vessel volume per minute), equipped with one spargers (unit length of about 1 meter), it is possible to derive the air velocity at the orifice level. Based on the fluids properties, the orifice diameter, and the air velocity, bubble diameter can be derived thanks to Shyu et al. work (Eq. (2)) [50]. The obtained value is 1.383 mm, which leads to a Bond number of 0.26. In addition to the value itself, its sensitivity is to be assessed, especially given the assumptions that were drawn. The most sensible part is the evaluation of the air velocity at the orifice level. Yet, to get a +5% deviation on the bubble diameter, one must increase the aeration from 0.1 to 277 vvm. Obtaining such a minor deviation for such an increase in the input flow rate shows the robustness of this estimation.

$$d = \sqrt[3]{\frac{(\pi + 1.31 Bo Fr) D^3}{Bo}} \tag{2}$$

where Fr is the Froude number, D is the orifice diameter. One should note that, fortunately, this correlation was validated for orifice diameters down to 60 μm.

The previous assumption also allows to evaluate the system void fraction. Based on a 0.155 m/s sliding velocity (see Supplementary Material), the void fraction can estimated at around 2.15%, which is too high to safely assume that bubbles will not collide. Therefore, O'Rourke's collision model was opted for (neglecting coalescence, though).

3.3. Numerical implementation

The CFD model was implemented into a homemade solver under OpenFOAM [51]. The code uses a PISO strategy (Pressure-Implicit with Splitting of Operators) to solve momentum and mass continuity equations. Initially, the system still has the bubble positions set randomly. The simulation is run so that the average sliding velocity enters a quasi-steady state (around 15 s) and is prolonged afterward (60 s) before extracting bubbles' locations. Bubble distribution was checked to be

relatively homogenous (*i.e.*, no artifact detected). Furthermore, the lack of apparent spatial correlation was also checked to ensure that the domain was large enough from a fluid dynamics point of view. All these elements are illustrated for the most dire case (assuming twice the anticipated void fraction) in the Supplementary Materials.

4. Light field model

Ray Tracing method coupled with Monte Carlo sampling was used to solve the Radiative Transport Equation (Eq. (3)) and compute the light field within the domain. In order to ease implementation, geometrical optics laws were used to describe rays' paths through the scene. Still, one should note that this assumption is relatively weak. Indeed, the lower limit of the validity of the geometrical optics assumption is given by two dimensionless numbers (ξ and p, Eqs. (4) and (5)), whose values should be greater than 1. More precisely, Dombrovskii advises them to be higher than 10 [46]. In this case, considering the largest wavelength of interest (800 nm), a refraction index of 1.33 for water and 1.0 for the air, the values of ξ and p are 10862 and 7169, respectively. Consequently, an approach based on geometrical optics can safely be developed. Furthermore, given the contrast of timescale between the three phenomena at stake (radiation - microseconds -, fluid flow - seconds -, and cell growth - hours to days -), a steady state approach can be used. Hence, for a given simulation, the cells are assumed not to evolve over the time required for the fluid flow to enter a pseudo-steady state, while the latter is assumed to be constant for the time required for the light field to propagate within the reactor.

$$\vec{s}.\nabla J_\lambda(\vec{x},\vec{s}) = -\sigma_{A,\lambda} C J_\lambda(\vec{x},\vec{s}) - \sigma_{S,\lambda} C J_\lambda(\vec{x},\vec{s}) + \frac{\sigma_{S,\lambda} C}{4\pi} \int_{4\pi} J_\lambda(\vec{x},\vec{s}_i) \Phi_\lambda(\vec{s}_i,\vec{s}) d\Omega_i \quad (3)$$

$$\xi = \frac{2\pi d}{\lambda} \quad (4)$$

$$p = 2\xi |m-1| \gg 1 \quad (5)$$

4.1. Ray tracing algorithm

Fig. 2 presents the Ray Tracing algorithm within a flowchart diagram. First, a starting position is randomly drawn (uniform distribution) on the lit external boundary of the domain. The rays are assumed to be collimated and normal to the boundary. Then, the distance to the next surface is determined. This surface can either a bubble or the domain bounding box. In addition, the distance to the next optical event (absorption or scattering) is drawn (an exponential distribution with the sum of the absorption and scattering coefficient as a parameter).

The two distances are then compared. If the distance to the event is the shortest, then the ray's position is updated to the event position, and the event nature is determined (uniform distribution, with the ratio of the absorption coefficient over the sum of the two as a parameter). If the ray is absorbed, its position is recorded, and the process starts anew. If the ray is scattered, a new direction is drawn from Henyey-Greenstein distribution [52] (with an anisotropy factor of 0.974, for *Chlorella vulgaris* [35]). Then, the process loops forward at the distance evaluation step.

If the distance comparison identifies that the next interaction is with a surface, two possible fates are discriminated. First, hitting the bounding box means that the ray escaped the computational domain. Consequently, the position at which it crossed the domain boundary is recorded, the simulation of this ray is terminated, and the process starts anew. Second, the ray interacts with a bubble. The angle of incidence (θ_i) and the possible angle of refraction (θ_r, Snell's law, refraction indices available in Table 1) are computed. Then, reflectivity is calculated assuming non-polarized light at a dielectric interface (Eq. (6)) [53]. Based on the obtained value, the nature of the interaction is drawn from a uniform distribution. Consequently, the ray's position is updated, and the new direction (reflection or refraction) is affected before the process loops forward at the distance evaluation step.

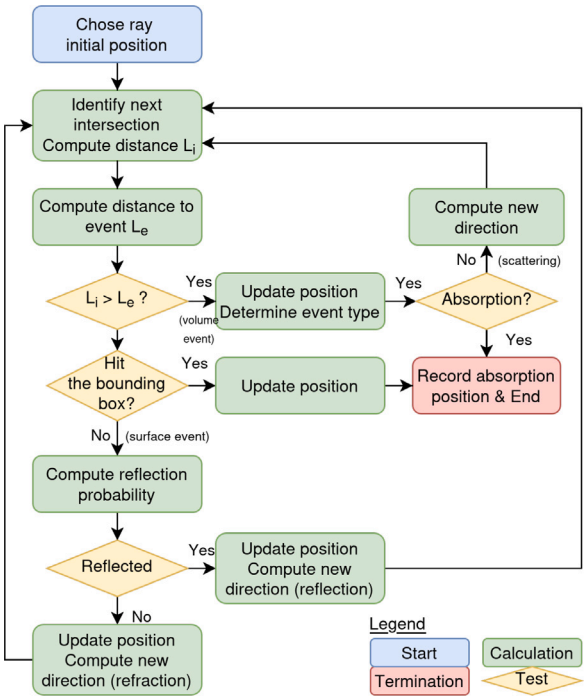

Fig. 2. Ray Tracing algorithm flowchart.

$$R_{interface} = \frac{1}{2}\left[\frac{\tan^2(\theta_i-\theta_r)}{\tan^2(\theta_i+\theta_r)} + \frac{\sin^2(\theta_i-\theta_r)}{\sin^2(\theta_i+\theta_r)}\right] \quad (6)$$

It should be noted that the simulations were led in a 3D scene. Still, given the fact that the setup is a 1D slab, it was possible to derive local absorption (at a given depth) by summing all the absorption events at the same depth within the slab. Going one step further, as incident rays are collimated, it is possible to reconstruct the local light field by subtracting the cumulated absorption (from the incident boundary) from the incident illumination. Finally, reflected and scattered away light can also be recorded in a straightforward manner.

4.2. Numerical implementation

A homemade code was developed based on the Star-Engine. Due to skill restriction, the code is CPU-bound, featuring C multithreading, though. As with any algorithm, it was mandatory to verify that results were unaffected by the numerical parameters. Therefore, the convergences of domain spatial subsampling (to avoid lateral boundary effects), the number of rays, and the number of scenes were led before producing simulations (taken as 50 bubble diameters, 150 millions rays, and one scene, respectively, see Supplementary Materials).

5. Tested conditions

While numerical tools are relevant, the explored conditions are even more important. In order to increase the generality of the findings and avoid discussing separately parameters that ultimately have the same contribution, a dimension analysis of the problem is to be conducted.

From a radiative perspective (the one of interest here), five physical quantities govern the system: the microalgae culture concentration (C, in kg/m^3), the cell absorption cross section (σ_A, in m^2/kg), the cell scattering cross section (σ_S, in m^2/kg), several characteristic lengths (which are taken as multiples of the bubble mean diameter d, in m),

Table 1
Properties defining the radiative scene and screened design space.

Parameter	Value/Range	Unit	Comment
d	1.383	mm	
n_{air}	1.00028276	–	[55]
$n_{culture}$	1.339	–	[56]
$n_{glazing}$	1.5082	–	Considered PMMA [57]
g	0.974	–	[35]
$\pi_1 = \frac{z}{d}$	[0, 100]	1	1000 points are distributed evenly (resolution 1/10 d)
$\pi_3 = \alpha$	[0, 0.043]	–	9 points are distributed evenly
$\pi_4 = C\sigma_A d$	[0.05, 1]	–	10 points are distributed evenly per decade (15 in total)
$\pi_5' = \frac{\sigma_S}{\sigma_A}$	[0.1, 50] & 0	–	10 points are distributed evenly per decade (24 in total)

the running depth (z, in m), the void fraction within the photobioreactor (α, no dimension), as well as the incident illumination (I_0 in μmolPhoton/m^2/s), and the illumination at the running depth ($I(z)$, in μmolPhoton/m^2/s). Therefore, according to Buckingham's π theorem, the system is governed by five dimensionless parameters.

The most obvious ones are the distance and light intensity ratios (π_1 and π_2), the void fraction (already dimensionless, π_3). Then come the absorption optical thickness (π_4) and the scattering optical thickness (π_5). Yet, one could also use the ratio of the cross sections as a second dimensionless number (π_5'). Indeed, its use further simplifies the system as its value is governed solely by biology, hence not a function of the primary operating conditions, that is, the cell concentration, nor bubble diameter. Consequently, the governing equation can be written as Eq. (8) or in a more application-oriented way as Eq. (9). This last manner of writing this equation highlights that the fraction of light impinging at the running depth is a function of the system absorption optical thickness, the scattering-to-absorption ratio, the bubble diameter, and the void fraction.

$$\pi_1 = \frac{z}{d}, \quad \pi_2 = \frac{I(z)}{I_0}, \quad \pi_3 = \alpha, \quad \pi_4 = \sigma_A C d, \quad \pi_5 = \sigma_S C d, \quad \pi_5' = \frac{\sigma_S}{\sigma_A} \tag{7}$$

$$f\left(\frac{z}{d}, \frac{\sigma_A}{\sigma_S}, \frac{I(z)}{I_0}, \alpha, C\sigma_A d\right) = 0 \tag{8}$$

$$\pi_2 = \frac{I(z)}{I_0} = g\left(\frac{z}{d}, \frac{\sigma_A}{\sigma_S}, \alpha, C\sigma_A d\right) \tag{9}$$

One could also have added the media refraction indices and their ratio to the list. Yet, as the setup is a photobioreactor, the gas–liquid system is thought to be restrained to an air–water system. Still, what is not fixed is the strain hosted within the bioreactor. In this system, changing the strain will change the scattering-to-absorption ratio (π_5') and its wavelength dependency. For example, *Chlorella vulgaris* (tiny coccoïd eukaryote) exhibits a scattering-to-absorption ratio between 6 and 50 [35,54], while it is below unity for *Anabaena variabilis* (filament-shape prokaryote) and varying from 0.1 to 0.5 [41].

In terms of values, ideally, π_1 should extend from 1 to infinite. Still, it was not possible from a hardware perspective (Dell Precision, Intel(R) Core(TM) i9-9880H CPU at 2.30 GHz, 64 Go RAM). Therefore, the domain was extended up to 100, *i.e.*, 100 times the bubble diameter. π_3 (*i.e.*, the void fraction) for taken as ranging from 0 to twice the value evaluated in the previous section (4.30%, *i.e.*, 2 × 2.15%). π_4 was investigated from 0.05 (very dilute culture) to unity (very concentrated culture). The lower bound was chosen to ensure the coherence of the radiative scene. Indeed, under the most conservative assumption in terms of ray penetration (no bubble, no scattering from microalgae), this value ensures that less than 1% escapes the scene. This argument is also a strong reason to favor π_4 over π_5. Finally, π_5' was preferred over π_5, as it is a biology-only number (characterizing the cell state, wavelength-wise), and the investigated ratio ranged from 0.1 to 50 (covering both *Chlorella vulgaris* and *Anabaena variabilis*). All these elements can be found in a summarized manner in Table 1. All in all, they amount to 3,240 runs constituting the database used in this work, requiring about two weeks to compute.

6. Results

6.1. Base case & general trend

Fig. 3 - Left - presents, in a logarithmic scale, the output of the Ray Tracing procedure without bubbles. It consists of the light absorption field within the domain for a selected combination of the dimensionless numbers governing the system. As one can see, the absorption profiles are influenced by the dimensionless parameters in a non-trivial manner. Nevertheless, it can be seen that relatively far from the illuminated boundary, the absorption profile becomes exponential (*i.e.*, linear in logarithmic scale). Also, the level of noise increases as the rays progress into the scene. This is a drawback of the MCMRT computational technique. Nevertheless, it is of minor importance here as the portions of the domain at stake are simply dark. From the local absorption field (Fig. 3 - Left), it is possible to recompute the local illumination field (Fig. 3 - Right, view field magnified from 0 to 25 bubble diameters to enhance the contrast). These profiles exhibit a similar shape as the ones encountered in literature [30]. They also differ from one another in the anticipated manner, which is a token of the reliability of the obtained results. For example, optical thickness (π_4, line pattern) is the first modulator of the spatial decrease of the light field (higher optical thickness leads to sharper decrease). Then, the relative amount of scattering (π_5', line color) is the second modulator. Very little difference can be observed for scattering-to-absorption ratio varying between 0.1 and 1. Then, as the relative amount of scattering increases, the profiles become steeper. It is explained by the lengthening of the effective ray path to reach a given depth, hence a higher chance of absorption on its way.

6.2. Illumination profile auto-similarity

Going one step further, it is possible to harness more of the dimensionless number power by leaving the π_2 versus π_1 plots at bay. Indeed, while convenient to analyze the results at first, that induces a loss of generality (*i.e.*, not following the guidance of Eq. (9)) by not accounting for the first order modulation that is the optical thickness (π_4). Taking the latter into consideration, plotting π_2 versus $\pi_1\pi_4$ allows to draw far more auto-similar profiles (Fig. 4 - Left). As one can see, this type of plot substantially reduces the dispersion originating from optical thickness. Indeed, it can be deemed that the optical thickness is, in this plot, a minor modulator compared to the scattering-to-absorption ratio (π_5'). Therefore, it is all the more natural to attempt the same procedure to reduce π_5' influence on the results. This time, an addition appears as an obvious scaling as scattering increases the effective ray path length. Consequently, an expression with the shape $\pi_1\pi_4(1 + \gamma\pi_5'^{\beta})$ was identified over the dataset (null void fraction). To do so, a Particle Swarm Optimizer coupled with a Genetic Algorithm was used (metric: Root Mean Squared Distance - RMSD - between the illumination profiles; for technical details, the reader is kindly referred to [58]). The first run of the optimizer yielded 0.02479 and 0.9848 for γ and β, respectively (plot available in Supplementary Materials). β being close to unity and conveying no meaning *per se*, a second procedure

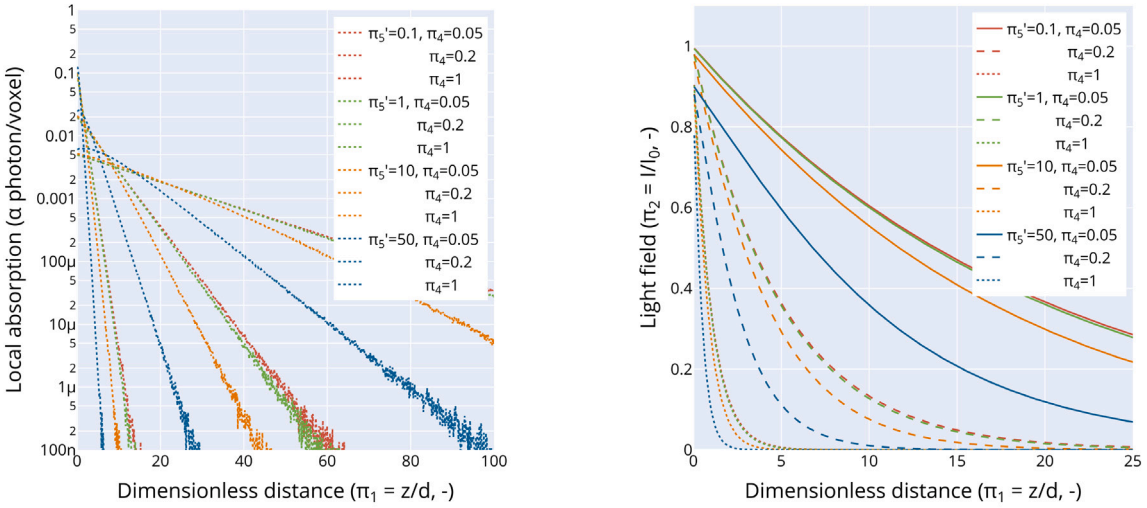

(a) Absorption field - No bubble

(b) Light field - No bubble

Fig. 3. Absorption field and light field within the domain without bubbles. Dimensionless abscissae.

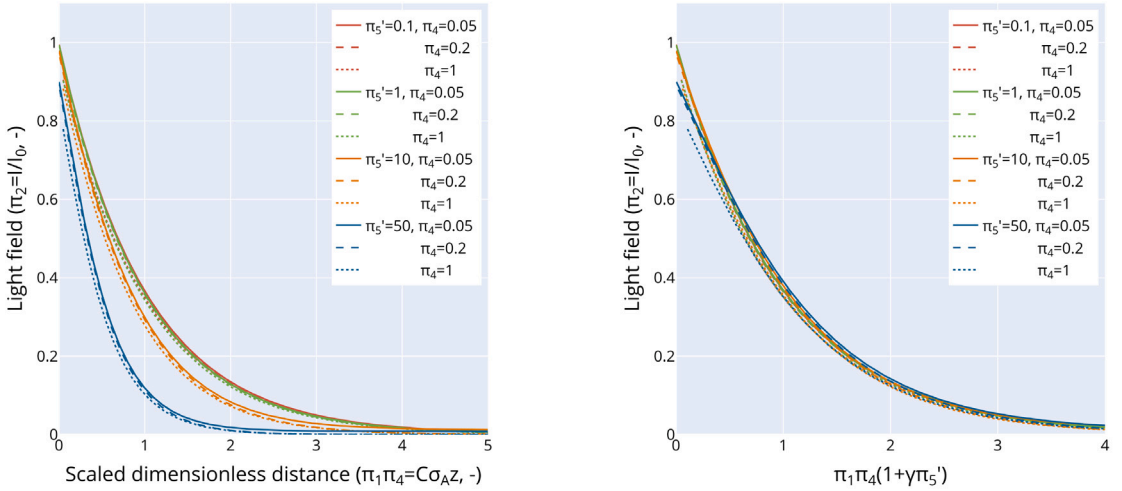

(a) Scaled by optical thickness

(b) Scaled by optical thickness and relative amount of scattering (with $\gamma = 0.02350$)

Fig. 4. Light field within the domain without bubbles. Scaled dimensionless abscissae.

was led, assuming $\beta = 1$. It yielded a value of 0.02350 for γ while simplifying the expression and reducing the number of parameters. Fig. 4 - Right - presents the results for the selected profiles. As one can see, they almost collapsed on the same line, which appears to follow a downward exponential trend.

An in-depth discussion of the potential meaning of the value of the γ coefficient seems in vain. Nevertheless, it is important to underline that from a conceptual point of view, the term $\gamma\pi_5'$ is the contribution of scattering the ray path lengthening. This lengthening pattern and the associated coefficient are not universal but case-dependent. Here, the underlying dependencies can be on the geometry and the scattering phase function (expression and coefficient). A different geometry, for example, a concentrating setup, such as a tube, would yield a different value for γ, even though the cells hosted by the culture would be the same. A different strain (*i.e.*, a different scattering phase function - expression and coefficient -) would also yield another γ value for the same setup. One can even expect that for the same phase function (Henyey-Greenstein), a lower asymmetry coefficient (g) value would lead to a higher γ value. Despite all these words of caution, it can be observed that even for the maximal value of π_5' (*i.e.*, 50), the scattering can only double the effective ray path length. This is a token of the robustness of the proposed expression. This robustness can be further evaluated by performing a sensitivity analysis. Indeed, if the γ coefficient is varied by ± 10%, the metric (RMSD) varies by +7.23/+8.95%, a good compromise between sensitivity and stability. From a biological perspective, it can be explained by the fact that the scattering phase function (with $g = 0.974$) is massively forward-oriented. Furthermore, in addition to mathematical robustness, the generality of the proposed expression is reinforced by the fact that a one-dimensional semi-infinite slab is a typical configuration and faithfully represents flat panel photobioreactors. At the same time, the choice of *Chlorella vulgaris* (g value in the Henyey-Greenstein phase function) echoes the fact that this strain is probably the most studied microalgae from a biotechnological point of view.

The final point of discussion of the bubble-free configuration is the overall trend of the auto-similar profile. Conceptually, if one accepts that the scaled dimensionless abscissa represents a proxy of the effective ray path length, then the trend should be a downward exponential.

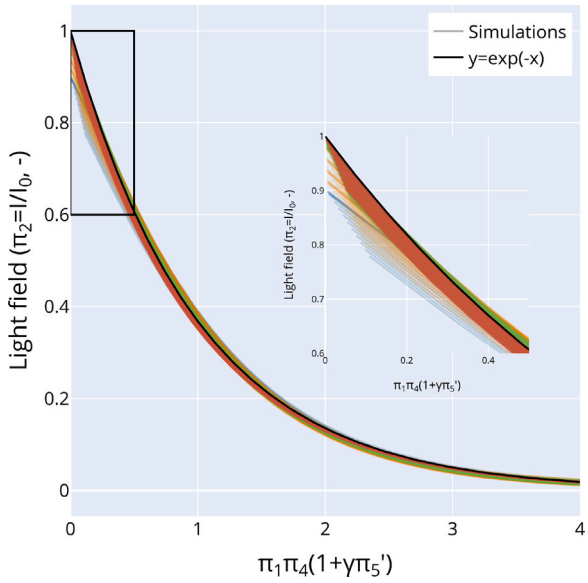

Fig. 5. Light field within the domain without bubbles for all the simulations and $I(z)/I_0 = exp(-\pi_1\pi_4(1+\gamma\pi_5'))$ curve. Scaled dimensionless abscissa (with γ = 0.02350).

Indeed, it is equivalent to assume that the complexity of the scattering terms of the Radiative Transport Equation (Eq. (3), two last terms) is lumped into the $(\gamma\pi_1\pi_4\pi_5')$ contribution. Therefore, it is possible to go one step further and guess that the resulting profile should have unity as the decay rate. All in all, it would yield a very simple expression: $I(z)/I_0 = exp(-\pi_1\pi_4(1+\gamma\pi_5'))$. Fig. 5 presents how this simple expression compares with all the simulations (360 in total, with π_4 varying from 0.05 to 1], π_5' from 0.1 to 50). As one can see, the suggested expression represents the upper bound of the simulated case. Nevertheless, the exponential trend with a unity decay appears to be adequate. Paying close attention, the reader can notice that the discrepancies originated from the initial value of the light field (abscissa of 0) (Fig. 5 - Inset). Indeed, by taking unity as the pre-exponential factor, one assumes that all the incident light penetrates the domain. While true when the relative scattering amount is low (*i.e.*, blue and red light), it is obviously wrong when scattering is dominating (*i.e.*, green light). This observation calls for a discussion on light sent back through the incident boundary (see next Section). Nevertheless, owing to its level of simplicity, the exponential profile with the unity decay model (or Beer–Lambert adequately corrected to account for scattering) provides a very satisfactory guess of the light profile.

6.3. Reflected light

The previous section underlined that a non-negligible quantity of incident illumination could be reflected and scattered away from the scene, especially in the case of a high scattering-to-absorption ratio. This state of fact bears two adverse consequences for the phycologist. First, not accounting for it would lead to a somewhat erroneous estimation of the local light field within the photobioreactor. Second, its omission could have a sizable impact on photosynthetic efficiency evaluation (a.k.a. PhotoConversion Efficiency - PCE). Indeed, overestimating the radiative energy actually supplied to the culture would lead to undervaluing the cell performance. This is especially true in the green part of the spectrum (about 1/3 of the Photosynthetically Active Radiation).

While complex to measure experimentally, accessing the amount of reflected light is relatively easy numerically. Fig. 6 - Left - presents the percentage of reflected light as a function of the two key dimensionless parameters π_4, the optical thickness, and π_5', the scattering-to-absorption ratio. When the three axes are scaled logarithmically, the dependence reveals itself. The optical thickness has no influence at all on the amount of the reflected light, while the scattering-to-absorption ratio controls it entirely. Even clearer is the linear dependence (in logarithmic scale) between the reflected fraction and the scattering-to-absorption ratio. An Ordinary Least Square regression on the whole dataset provides an almost perfectly linear dependency to the reflected light fraction (ρ) with the scattering-to-absorption ratio (Eqs. (10) and (11)).

$$ln(\rho) = 1.049\ 10^{-2}\ ln(\pi_5') - 6.489 \qquad R^2 = 0.9996, p = 0.0000 \tag{10}$$

$$\rho = 1.520\ 10^{-3}\ \pi_5'^{1.049} \tag{11}$$

Here again, given that the exponent is close to unity, it is possible to reduce the number of parameters and provide a simpler equation. With this approach, the reflected and scattered away light fraction can be written as:

$$\rho = 1.888\ 10^{-3}\ \pi_5' \tag{12}$$

With light reflection and scattering modeled, the next step is to reevaluate the capability of the exponential decay model to describe the light profiles. Out of fairness, the γ value was optimized again to minimize RMSD. This time, the obtained value is 0.02046, which is close to the previous one and does not alter the previous discussion associated with it. Fig. 6 - Right - displays the projection of the dataset and the unity exponential decay. As one can see, the match is quite good. Moving from mere observation to quantification, the Mean Absolute Relative Error (MARE), which measures the average local relative deviation on the profile, is 5.10%, on the 360 profiles. Taking the relative difference in overall absorbed energy as a less stringent, still relevant, criterion, the deviation is established at 2.17%. One should note that these indicators were computed on 95% of total energy (*i.e.*, until $\pi_1\pi_4$ reaches 3) to prevent a long tailing effect from biasing the metrics. All in all, this procedure yields a very simple Beer–Lambert-like expression accounting in an explainable manner for light reflection and scattering outside of the domain and effective ray path length (Eq. (13)).

$$\frac{I(z)}{I_0} = (1 - \underbrace{\phi(\frac{\sigma_S}{\sigma_A})}_{\substack{\text{Reflection}\\ \text{away}}})exp(-\sigma_A C \underbrace{z(1+\gamma\frac{\sigma_S}{\sigma_A})}_{\substack{\text{Effective ray}\\ \text{path length}}}) \tag{13}$$

with $\phi = 1.888\ 10^{-3}$ and $\gamma = 0.02046$.

6.4. Effects of bubbles

6.4.1. General trend

Once the bubble-free phenomena have been examined and discussed, it is time to deal with the effect of bubbles on the light field and its modeling. In order to get a grasp of the spatial distributions, Fig. 7 - Left - presents the illumination profiles in the actual spatial space. As one can see, bubbles addition induces two effects. First, it shifts the profiles downward. This effect is all the more pronounced as optical thickness is low. Second, and less evident to notice, is the increase of the reflected light. Both can be explained by the additional scattering induced by the presence of the bubbles, as already noticed by others authors [41,46]. In the same processing approach as previously, the profiles were scaled against the contribution of optical thickness and scattering-to-absorption ratio (Fig. 7 - Right). For the sake of simplicity and to avoid uninteresting lengthening of this article, the scaling was performed with the γ parameter obtained without bubble and without accounting for the light reflected (and scattered) away (optimization procedure to be led afterwards). As one can see, this scaling it still

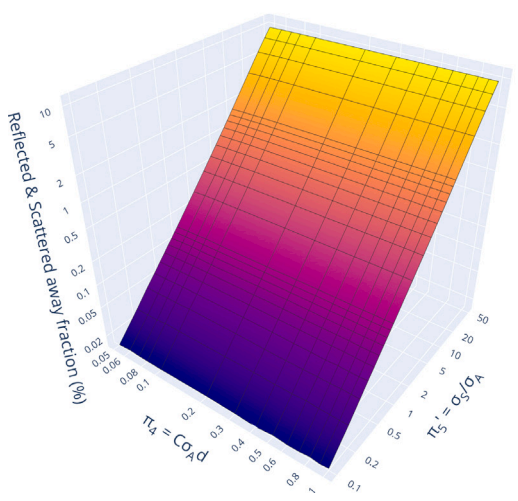

(a) Reflected light

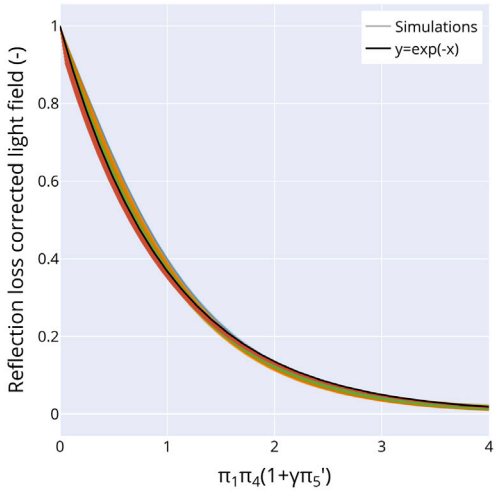

(b) Scaled by optical thickness and relative amount of scattering (with $\gamma = 0.02046$)

Fig. 6. Left - Reflected and scattered light response surface, without bubble (logarithmic scale on all axis). Surface color is equivalent to z axis. Right - Light field corrected by reflection loss within the domain without bubbles. Scaled dimensionless abscissa, 360 profiles.

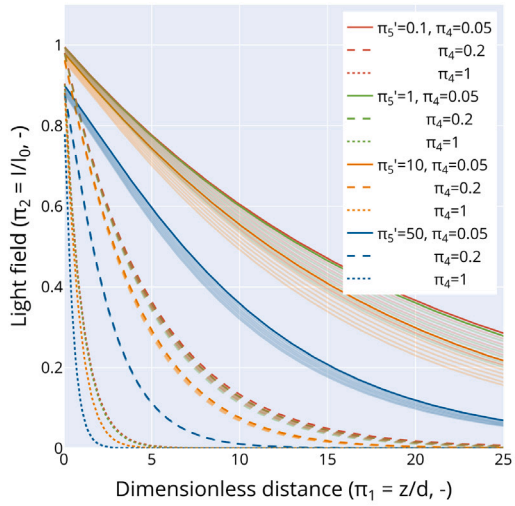

(a) Light field - No scaling

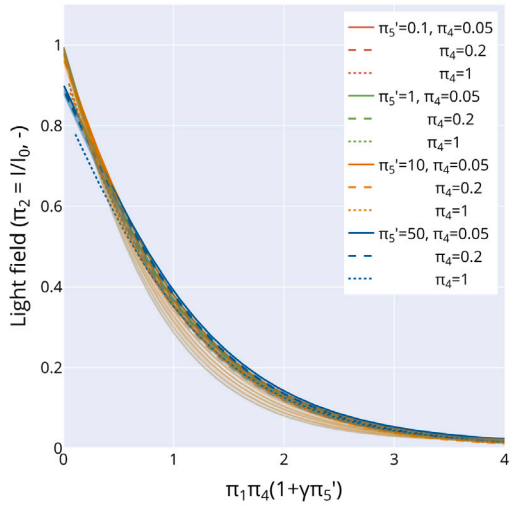

(b) Scaled by optical thickness and relative amount of scattering

Fig. 7. Light field within the domain for the different void fraction. Solid lines - 0% void fraction. Translucent lines - varying void fractions. Standard and scaled dimensionless abscissae (with $\gamma = 0.02350$).

relevant and underlines that the light profile auto-similarity is not voided by the presence of bubbles.

The next step is, therefore, to investigate the effect of the void fraction and its induced scattering on the light reflected and scattered away from the scene. Fig. 8 presents two three-dimensional views of the reflected and scattered fraction of the incident light versus the optical thickness and the scattering-to-absorption ratio. From an intuitive point of view, these response surfaces are the sums of two planes, one inclined with π_5' (like in the bubble-free case) and one inclined with π_4. This intuition is supported by the manner in which the Radiative Transport Equation is written in order to account for the presence of bubbles (Eq. (14)), assuming bubbles do not absorb radiation. Indeed, the bubble contribution is additive. Furthermore, it is important to note that the introduction of the void fraction will lower the effective participation of the culture to the light distribution ($1-\alpha$ term) [41,46].

$$\begin{aligned}\vec{s}.\nabla J_\lambda(\vec{x},\vec{s}) = &-(1-\alpha)\sigma_{A,\lambda}CJ_\lambda(\vec{x},\vec{s}) - (1-\alpha)\sigma_{S,\lambda}CJ_\lambda(\vec{x},\vec{s}) \\ &+ (1-\alpha)\frac{\sigma_{S,\lambda}C}{4\pi}\int_{4\pi} J_\lambda(\vec{x},\vec{s}_i)\Phi_\lambda(\vec{s}_i,\vec{s})d\Omega_i \\ &- \frac{3\alpha}{4d}\sigma_{S,\lambda,b}J_\lambda(\vec{x},\vec{s}) + \frac{3\alpha}{4d}\frac{\sigma_{S,\lambda,b}}{4\pi}\int_{4\pi} J_\lambda(\vec{x},\vec{s}_i)\Phi_{\lambda,b}(\vec{s}_i,\vec{s})d\Omega_i\end{aligned} \tag{14}$$

6.4.2. Reflected and scattered away light

Consequently, in order to untangle the two scattering contributions, the focus was set on a specific case: $\pi_5' = 0$, *i.e.*, microalgae not scattering, allowing to isolate bubble-only contribution (Fig. 9 - Left). As one can see, the fraction of light reflected and scattered away evolved in an almost bilinear manner. It can be considered as the combination of two independent trends, one function of the void fraction, the other

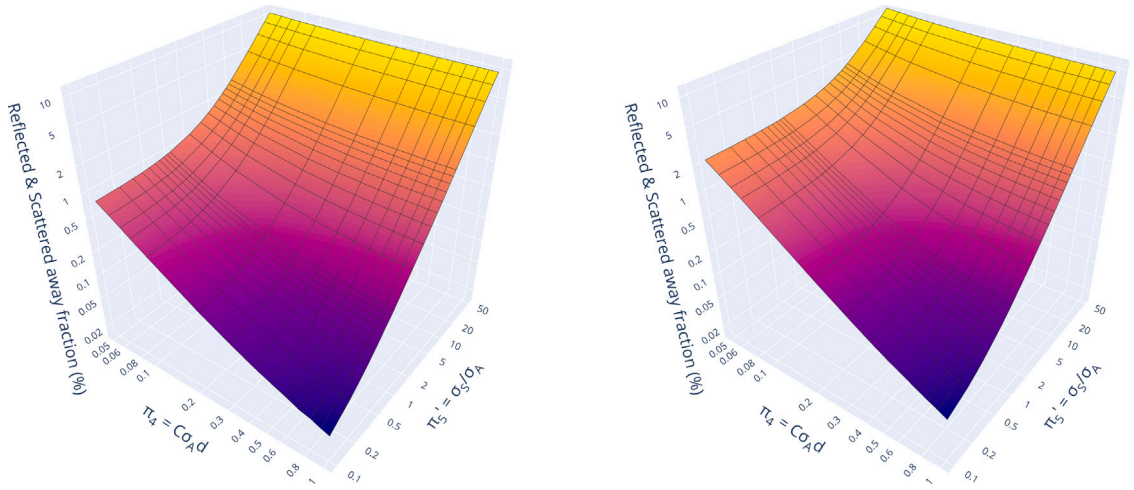

(a) 2.15 % void fraction (b) 4.30 % void fraction

Fig. 8. Reflected and scattered light response surfaces for median and high void fractions. Surface color is equivalent to z axis.

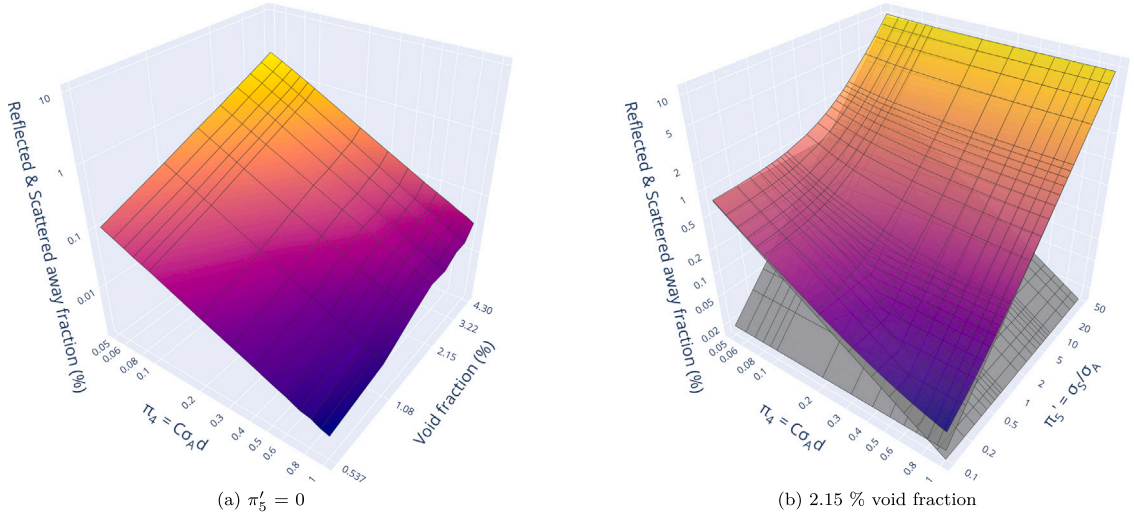

(a) $\pi_5' = 0$ (b) 2.15 % void fraction

Fig. 9. Left - Reflected and scattered light response surface as a function of void fraction and optical thickness. Microalgae scattering was nullified, *i.e.*, $\pi_5' = 0$. Right - Reconstructed reflected light fraction (colored surface) based on the sum of the bubbles and cells scattering (gray surfaces) for the median void fraction. To be compared with Fig. 8 - Left. Surface color is equivalent to z axis.

of the optical thickness. Still, modulations have to be brought to this statement. First, the dependency on the void fraction marks hints of the potential appearance of higher-order terms for high void fractions. This observation aligns with Dombrovskii's comment that linear dependency is only valid for low void fractions without proposing a correction for higher fractions though [46]. In addition, the keen observer will notice that the shape of the response surface tends to get rough for high optical thickness. It can be explained by the fact that at high optical thickness, the number of bubbles encountered by the rays diminishes until not enough are interacted with to offer a stable estimate. With these two observations in mind, a mathematical description of the bubbles' contribution to reflected and scattered light was intended.

A multilinear regression was led in logarithmic space to minimize the RMSD in the $\pi_4 \times \alpha$ space. After some rationalization and transformation back into the linear space, the fraction of light reflected and scattered by the bubbles can be modeled as Eq. (15). The quality of the agreement is particularly good (see Supplementary Materials), with a MARE of 6.35% (culled below 0.1% of reflected light to avoid a long tailing effect). Therefore, the overall effect of the void fraction and the cell scattering-to-absorption ratio can be reconstructed. Fig. 9 - Right - presents the reconstructed response surface (colored surface) and the two underlying components (gray surfaces) for a void fraction of 2.15% (median case). It is possible to assess the efficacy of the process by comparing the results with Fig. 8 - Left.

$$\rho_b = 2.365\ 10^{-2}\ (\frac{\alpha}{\pi_4})^{4/3} \tag{15}$$

6.4.3. Profile auto-similarity

Once reflection and scattering out of the domain have been accounted for, the next step was to describe the lengthening of the ray path originating from bubble-induced scattering. On this point, three comments have to be drawn. First of all, the effect of bubble-induced scattering is additive (Eq. (14)), and the formulation should reflect this state of fact. Second, the presence of bubbles reduces the effective absorption of the medium (π_4 dimensionless number) but not the microalgae strain properties (π_5' unchanged). Third, in the same manner as for reflection, the optical thickness (π_4) interplays with bubble effects on ray paths effective length. Indeed, the higher the optical thickness, the lower the amount of interaction with the bubbles. The modulation of the interaction can be assumed to be reasonably described by a decaying exponential function of the optical thickness. All these considerations lead to the formulation suggested in Eq. (16).

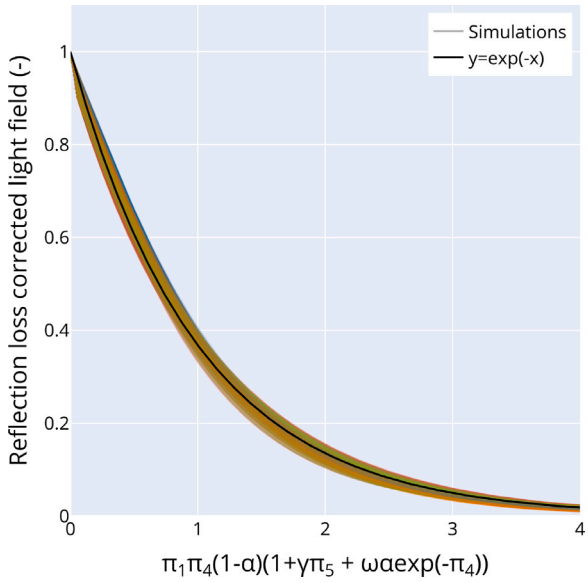

Fig. 10. Light field corrected by reflection loss within the domain without bubbles. Scaled dimensionless abscissa (with γ = 0.02046 and ω = 5.830), 3,240 profiles.

With the equation suggested, the next step is to evaluate the capability of the correlation to describe the light profiles. The ω value was optimized to minimize RMSD. The obtained value for ω is 5.830. Fig. 10 presents the projection of the whole dataset (3,240 profiles) and the model. As one can see, the match is quite good. The MARE is 9.50% (local deviation), and the relative difference in overall absorbed energy is 2.25%. Given the span of the dataset in terms of optical thickness (proxy of concentration), scattering-to-absorption ratio (proxy of cell strain and pigment profile), and void fraction, the simplicity of the proposed correlation performs remarkably well.

$$\frac{I(z)}{I_0} = (1 - \underbrace{\phi\left(\frac{\sigma_S}{\sigma_A}\right)}_{\text{Reflection by the cells}} - \underbrace{\zeta\left(\frac{\alpha}{\sigma_A C d}\right)^{4/3}}_{\text{Reflection by the bubbles}}) \times exp(-\sigma_A C z) \underbrace{(1-\alpha)}_{\text{Bubble effect on absorption}} (1 + \underbrace{\gamma\frac{\sigma_S}{\sigma_A}}_{\text{Cell ray path lengthening}} + \underbrace{\omega\alpha\ exp(-\sigma_A C d)}_{\text{Bubble ray path lengthening}}) \quad (16)$$

with ϕ = 1.888 10^{-3}, ζ = 2.365 10^{-2}, γ = 0.02046, and ω = 5.830.

7. Applicability & perspectives

The present work offers an easy-to-use approach to computing the light profile within a photobioreactor. It only requires one to know the absorption coefficient and its scattering counterpart for a given wavelength. With them, it is also possible to access the amount of light reflected and scattered towards the surroundings and adjust the energy balance accordingly. In addition, volume averaging of the light to evaluate the global production rate would be more accurate (owing to the saturating effect in the irradiance-photosynthesis curve). Furthermore, using a correlation is undoubtedly easier to handle and faster to compute than any other methods (Discrete Ordinate Method, Pn approximation, Ray Tracing, etc.) or other surrogate modeling methods (such as machine learning or AI algorithms, whose deployability is sometimes hindered by the restricted availability of the model parameter and/or training data). It is possible to envision broadcasting the detailed knowledge it bears to a larger scale, such as a photobioreactor field or the country scale, to ascertain photosynthetic energy balance.

For example, let us consider a baffled airlift photobioreactor with a depth of 5 cm and a recirculation frequency around 1 Hz. Assuming a sinusoidal motion, one can determine the position of a microalgae cell within the photobioreactor over time. Adding to this, the light field, computed with the proposed correlation, one can obtain the light cycle experienced by the cell. Fig. 11 illustrates this for a culture of *Chlorella vulgaris* at different concentrations and for two bands of the visible spectrum (blue and green). From the left graph, one can see that the light penetration is modulated by both concentration and color, with green light escaping the photobioreactor for the lowest concentration, while blue light is almost entirely absorbed. Consequently, the experienced light cycle, on the right graph, has a decreasing duty cycle whose amplitude is substantially modulated by the light color.

In terms of perspectives, this work calls for further research effort. For example, the fluid dynamics aspect could be enhanced by simulating a setup featuring actual glazing (wall boundary condition instead of cyclic) and all the associated complexity (*e.g.*, wall lift force) [39,59]. Then, bubble diameter could be drawn out of a distribution instead of set at a fixed value. In terms of illumination calculation, diffuse and oblique incident radiation should also be explored to complement the current setup. Exploring all these refinements would make the simulations closer to an actual setup and allow to weigh the relative importance of the difference between the phenomena. Therefore, it would be possible to rank them in terms of contributions and relevance.

8. Conclusion

This work computed using Ray Tracing coupled with Monte Carlo Method, the light field within a photobioreactor featuring physics-accurately distributed bubbles for 3240 configurations (cell concentrations, strains, pigment profiles, void fraction, etc.). From a physical perspective, this investigation showed that the presence of bubbles lengthens the ray path within the culture medium and increases the apparent absorption. In addition, a sizable amount of the incident light can be reflected and scattered away (about 10% for a 2.15% void fraction). From a numerical perspective, using a dimensionless approach, the whole knowledge of the database was condensed into an exponential decay (Beer–Lambert-like) model. It allows to compute local light field with an accuracy of 9.50%, and distributed energy with a 2.25% accuracy. While this work is only a first step calling for more detailed investigations (wall effect, bubble size distribution, etc.), its simplicity and computational efficiency allow to be used to precisely account for detailed light distribution in large-scale models, improving the computation of country-scale microalgae cultivation performances.

Declaration of competing interest

The authors declare that they have no known competing financial interests or personal relationships that could have appeared to influence the work reported in this paper.

Acknowledgments

The author would like to thank Olivier Louisnard for opening the world of dimensionless numbers to him. This project was funded by the French government as part of the France 2030 initiative. Communauté urbaine du Grand Reims, Département de la Marne, Région Grand Est and European Union (FEDER Grand Est 2021–2027) are acknowledged for their financial support to the Chair of Biotechnology of CentraleSupélec and the Centre Européen de Biotechnologie et de Bioéconomie (CEBB).

Appendix A. Supplementary data

Supplementary material related to this article can be found online at https://doi.org/10.1016/j.algal.2025.104331.

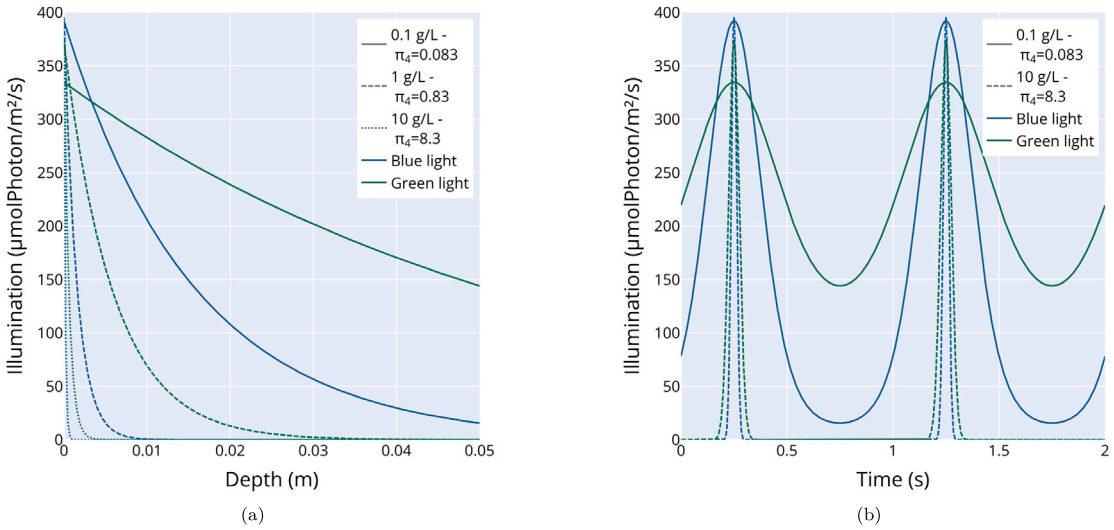

Fig. 11. Left - Illumination profiles within the photobioreactor for different microalgae concentrations and colors. Right - Light history experienced by a *Chlorella vulgaris* cell for different microalgae concentrations and colors (1 g/L concentration intentionally omitted for readability reasons). Biological properties, for the blue color $\sigma_A = 600$ kg/m^2, $\sigma_S = 3500$ kg/m^2, for the green color $\sigma_A = 100$ kg/m^2, $\sigma_S = 3500$ kg/m^2. Incident illumination (I_0) of 400 µmolPhoton/m^2/s.

Data availability

No data was used for the research described in the article.

References

[1] S. Diaz, J. Settele, E. Brondizio, H.T. Ngo, M. Guèze, J. Agard, C. Zayas, IPBES global assessment: summary for policymakers, 2019, Retrieved from IPBES website https://www.ipbes.net/news/ipbes-global.

[2] R.H. Eckel, S.M. Grundy, P.Z. Zimmet, The metabolic syndrome, Lancet 365 (9468) (2005) 1415–1428, http://dx.doi.org/10.1016/S0140-6736(05)66378-7, URL https://www.sciencedirect.com/science/article/pii/S0140673605663787.

[3] A.K. Koyande, K.W. Chew, K. Rambabu, Y. Tao, D.-T. Chu, P.-L. Show, Microalgae: A potential alternative to health supplementation for humans, Food Sci. Hum. Wellness 8 (1) (2019) 16–24, http://dx.doi.org/10.1016/j.fshw.2019.03.001, URL https://www.sciencedirect.com/science/article/pii/S2213453018301435.

[4] M.S. Madeira, C. Cardoso, P.A. Lopes, D. Coelho, C. Afonso, N.M. Bandarra, J.A.M. Prates, Microalgae as feed ingredients for livestock production and meat quality: A review, Livest. Sci. 205 (2017) 111–121, http://dx.doi.org/10.1016/j.livsci.2017.09.020, URL https://www.sciencedirect.com/science/article/pii/S1871141317302858.

[5] W. Levasseur, P. Perré, V. Pozzobon, A review of high value-added molecules production by microalgae in light of the classification, Biotech. Adv. 41 (2020) 107545, http://dx.doi.org/10.1016/j.biotechadv.2020.107545, URL http://www.sciencedirect.com/science/article/pii/S0734975020300422.

[6] C. Camarena-Bernard, V. Pozzobon, Evolving perspectives on lutein production from microalgae - a focus on productivity and heterotrophic culture, Biotech. Adv. (2024) 108375, http://dx.doi.org/10.1016/j.biotechadv.2024.108375, URL https://www.sciencedirect.com/science/article/pii/S0734975024000697.

[7] H. Chen, Q. Wang, Microalgae-based nitrogen bioremediation, Algal Res. 46 (2020) 101775, http://dx.doi.org/10.1016/j.algal.2019.101775, URL https://www.sciencedirect.com/science/article/pii/S2211926419311233.

[8] V. Pozzobon, N. Cui, A. Moreaud, E. Michiels, W. Levasseur, Nitrate and nitrite as mixed source of nitrogen for Chlorella vulgaris: Growth, nitrogen uptake and pigment contents, Bioresour. Technol. (2021) 124995, http://dx.doi.org/10.1016/j.biortech.2021.124995, URL https://www.sciencedirect.com/science/article/pii/S0960852421003345.

[9] M.K. Enamala, S. Enamala, M. Chavali, J. Donepudi, R. Yadavalli, B. Kolapalli, T.V. Aradhyula, J. Velpuri, C. Kuppam, Production of biofuels from microalgae - a review on cultivation, harvesting, lipid extraction, and numerous applications of microalgae, Renew. Sustain. Energy Rev. 94 (2018) 49–68, http://dx.doi.org/10.1016/j.rser.2018.05.012, URL http://www.sciencedirect.com/science/article/pii/S1364032118303551.

[10] E. Posadas, M.d.M. Morales, C. Gomez, F.G. Acién, R.l. Muñoz, Influence of pH and CO2 source on the performance of microalgae-based secondary domestic wastewater treatment in outdoors pilot raceways, Chem. Eng. J. 265 (2015) 239–248, http://dx.doi.org/10.1016/j.cej.2014.12.059, URL https://www.sciencedirect.com/science/article/pii/S1385894714016738.

[11] J.s. Ruiz, G. Olivieri, J.d. Vree, R. Bosma, P. Willems, J.H. Reith, M.H.M. Eppink, D.M.M. Kleinegris, R.H. Wijffels, M.J. Barbosa, Towards industrial products from microalgae, Energy Environ. Sci. 9 (10) (2016) 3036–3043, http://dx.doi.org/10.1039/C6EE01493C, Publisher: The Royal Society of Chemistry. URL https://pubs.rsc.org/en/content/articlelanding/2016/ee/c6ee01493c.

[12] B. Porto, T. F.C.V. Silva, A.L. Gonçalves, A.F. Esteves, S.M.A.G.U. de Souza, A.A.U. de Souza, J.C.M. Pires, V.J.P. Vilar, Tubular photobioreactors illuminated with LEDs to boost microalgal biomass production, Chem. Eng. J. 435 (2022) 134747, http://dx.doi.org/10.1016/j.cej.2022.134747, URL https://www.sciencedirect.com/science/article/pii/S1385894722002558.

[13] G. Luzi, C. McHardy, C. Lindenberger, C. Rauh, A. Delgado, Comparison between different strategies for the realization of flashing-light effects Pneumatic mixing and flashing illumination, Algal Res. 38 (2019) 101404, http://dx.doi.org/10.1016/j.algal.2018.101404, URL http://www.sciencedirect.com/science/article/pii/S2211926418306520.

[14] J. Pruvost, B. Le Gouic, O. Lepine, J. Legrand, F. Le Borgne, Microalgae culture in building-integrated photobioreactors: Biomass production modelling and energetic analysis, Chem. Eng. J. 284 (2016) 850–861, http://dx.doi.org/10.1016/j.cej.2015.08.118, URL https://www.sciencedirect.com/science/article/pii/S1385894715012012.

[15] K. Liffman, D.A. Paterson, P. Liovic, P. Bandopadhayay, Comparing the energy efficiency of different high rate algal raceway pond designs using computational fluid dynamics, Chem. Eng. Res. Des. 91 (2) (2013) 221–226, http://dx.doi.org/10.1016/j.cherd.2012.08.007, URL https://www.sciencedirect.com/science/article/pii/S0263876212003048.

[16] I. Perner-Nochta, C. Posten, Simulations of light intensity variation in photobioreactors, J. Biotech. 131 (3) (2007) 276–285, http://dx.doi.org/10.1016/j.jbiotec.2007.05.024, URL http://www.sciencedirect.com/science/article/pii/S0168165607003720.

[17] C. Qin, J. Wu, Influence of successive and independent arrangement of Kenics mixer units on light/dark cycle and energy consumption in a tubular microalgae photobioreactor, Algal Res. 37 (2019) 17–29, http://dx.doi.org/10.1016/j.algal.2018.09.020, URL http://www.sciencedirect.com/science/article/pii/S2211926417308299.

[18] C. Qin, J. Wu, J. Wang, Synergy between flow and light fields and its applications to the design of mixers in microalgal photobioreactors, Biotechnol. Biofuels 12 (1) (2019) 93, http://dx.doi.org/10.1186/s13068-019-1430-y.

[19] P. Hartmann, D. Demory, C. Combe, R. Hamouda, A.-C. Boulanger, M.-O. Bristeau, J. Sainte-Marie, B. Sialve, J.-P. Steyer, S. Rabouille, A. Sciandra, O. Bernard, Growth Rate Estimation of algae in Raceway Ponds: A novel Approach, 19th IFAC World Congress, IFAC Proc. Vol. 47 (3) (2014) 6216–6221, http://dx.doi.org/10.3182/20140824-6-ZA-1003.02408, URL http://www.sciencedirect.com/science/article/pii/S1474667016425863.

[20] M.J. Barbosa, M. Janssen, N. Ham, J. Tramper, R.H. Wijffels, Microalgae cultivation in air-lift reactors: Modeling biomass yield and growth rate as a function of mixing frequency, Biotechnol. Bioeng. 82 (2) (2003) 170–179, http://dx.doi.org/10.1002/bit.10563, _eprint: https://onlinelibrary.wiley.com/doi/pdf/10.1002/bit.10563. URL https://onlinelibrary.wiley.com/doi/abs/10.1002/bit.10563.

[21] J. Degen, A. Uebele, A. Retze, U. Schmid-Staiger, W. Trösch, A novel airlift photobioreactor with baffles for improved light utilization through the flashing light effect, Biochemical Engineering: Trends and Potentials, J. Biotech. 92 (2) (2001) 89–94, http://dx.doi.org/10.1016/S0168-1656(01)00350-9, URL https://www.sciencedirect.com/science/article/pii/S0168165601003509.

[22] W. Trösch, U. Schmid-Staiger, A. Zastrow, A. Retze, F. Brucker, Photobioreactor with improved supply of light by surface enlargement, wavelength shifter bars or light transport, 2003, URL https://patents.google.com/patent/US6509188B1/en.

[23] J. Huang, F. Feng, M. Wan, J. Ying, Y. Li, X. Qu, R. Pan, G. Shen, W. Li, Improving performance of flat-plate photobioreactors by installation of novel internal mixers optimized with computational fluid dynamics, Bioresour. Technol. 182 (2015) 151–159, http://dx.doi.org/10.1016/j.biortech.2015.01.067, URL https://www.sciencedirect.com/science/article/pii/S0960852415000875.

[24] X. Gao, B. Kong, R. Dennis Vigil, Comprehensive computational model for combining fluid hydrodynamics, light transport and biomass growth in a Taylor vortex algal photobioreactor: Eulerian approach, Algal Res. 24 (2017) 1–8, http://dx.doi.org/10.1016/j.algal.2017.03.009, URL https://www.sciencedirect.com/science/article/pii/S2211926416303563.

[25] T. Sato, D. Yamada, S. Hirabayashi, Development of virtual photobioreactor for microalgae culture considering turbulent flow and flashing light effect, Energy Convers. Manage. 51 (6) (2010) 1196–1201, http://dx.doi.org/10.1016/j.enconman.2009.12.030, URL http://www.sciencedirect.com/science/article/pii/S0196890409005366.

[26] F.P. Incropera, J.F. Thomas, A model for solar radiation conversion to algae in a shallow pond, Sol. Energy 20 (2) (1978) 157–165, http://dx.doi.org/10.1016/0038-092X(78)90189-5, URL https://www.sciencedirect.com/science/article/pii/0038092X78901895.

[27] A. Saccardo, A. Porcelli, L. Borella, E. Sforza, F. Bezzo, Model-based optimisation of microalgae growth under high-intensity and high-frequency pulsed light conditions, J. Clean. Prod. 469 (2024) 143238, http://dx.doi.org/10.1016/j.jclepro.2024.143238, URL https://www.sciencedirect.com/science/article/pii/S0959652624026878.

[28] E.M. Grima, F.G. Camacho, J.A.S. Pérez, J.M.F. Sevilla, F.G.A. Fernandez, A.C. Gómez, A mathematical model of microalgal growth in light-limited chemostat culture, J. Chem. Technol. Biotechnol. 61 (2) (1994) 167–173, http://dx.doi.org/10.1002/jctb.280610212, _eprint: https://onlinelibrary.wiley.com/doi/pdf/10.1002/jctb.280610212. URL https://onlinelibrary.wiley.com/doi/abs/10.1002/jctb.280610212.

[29] V. Pozzobon, P. Perré, Multiscale numerical workflow describing microalgae motion and light pattern incidence towards population growth in a photobioreactor, J. Theoret. Biol. 498 (2020) 110293, http://dx.doi.org/10.1016/j.jtbi.2020.110293, URL https://www.sciencedirect.com/science/article/pii/S002251932030148X.

[30] J.F. Cornet, C.G. Dussap, G. Dubertret, A structured model for simulation of cultures of the cyanobacterium Spirulina platensis in photobioreactors: I. Coupling between light transfer and growth kinetics, Biotechnol. Bioeng. 40 (7) (1992) 817–825, http://dx.doi.org/10.1002/bit.260400709, _eprint: https://onlinelibrary.wiley.com/doi/pdf/10.1002/bit.260400709. URL https://onlinelibrary.wiley.com/doi/abs/10.1002/bit.260400709.

[31] A. Schuster, Radiation through a foggy atmosphere, Astrophys. J. Vol. 21, P. 1 21 (1905) 1, ISBN: 0004-637X.

[32] J.F. Cornet, C.G. Dussap, J.B. Gros, C. Binois, C. Lasseur, A simplified monodimensional approach for modeling coupling between radiant light transfer and growth kinetics in photobioreactors, Chem. Eng. Sci. 50 (9) (1995) 1489–1500, http://dx.doi.org/10.1016/0009-2509(95)00022-W, URL https://www.sciencedirect.com/science/article/pii/000925099500022W.

[33] A.M. Elmalky, M.T. Araji, Optimization models for photosynthetic bioenergy generation in building façades, Renew. Energy 228 (2024) 120607, http://dx.doi.org/10.1016/j.renene.2024.120607, URL https://www.sciencedirect.com/science/article/pii/S096014812400675X.

[34] J. Hoeniges, W. Welch, J. Pruvost, L. Pilon, A novel external reflecting raceway pond design for improved biomass productivity, Algal Res. 65 (2022) 102742, http://dx.doi.org/10.1016/j.algal.2022.102742, URL https://www.sciencedirect.com/science/article/pii/S2211926422001138.

[35] R. Kandilian, A. Soulies, J. Pruvost, B. Rousseau, J. Legrand, L. Pilon, Simple method for measuring the spectral absorption cross-section of microalgae, Chem. Eng. Sci. 146 (2016) 357–368, http://dx.doi.org/10.1016/j.ces.2016.02.039, URL https://www.sciencedirect.com/science/article/pii/S0009250916300938.

[36] B. Kong, R.D. Vigil, Simulation of photosynthetically active radiation distribution in algal photobioreactors using a multidimensional spectral radiation model, Bioresour. Technol. 158 (2014) 141–148, http://dx.doi.org/10.1016/j.biortech.2014.01.052, URL https://www.sciencedirect.com/science/article/pii/S0960852414000777.

[37] J. Hoeniges, Theoretical and experimental investigation of light and culture intensification in solar microalgae cultivation systems (Ph.D. thesis), Nantes Université, 2023.

[38] Y.A. Lim, I.M.S.K. Ilankoon, M.N. Chong, S.C. Foo, Improving microalgae growth and carbon capture through micro-size bubbles generation in flat-panel photobioreactors: Impacts of different gas sparger designs on mixing performance, Renew. Sustain. Energy Rev. 171 (2023) 113001, http://dx.doi.org/10.1016/j.rser.2022.113001, URL https://www.sciencedirect.com/science/article/pii/S1364032122008826.

[39] K. Felton, E. Loth, Spherical bubble motion in a turbulent boundary layer, Phys. Fluids 13 (9) (2001) 2564–2577, http://dx.doi.org/10.1063/1.1388051.

[40] H.C. Hulst, Light Scattering by Small Particles, Wiley, 1957, Google-Books-ID YtwNAQAAIAAJ.

[41] H. Berberoglu, J. Yin, L. Pilon, Light transfer in bubble sparged photobioreactors for H2 production and CO2 mitigation, ICHS-2005, Int. J. Hydrog. Energy 32 (13) (2007) 2273–2285, http://dx.doi.org/10.1016/j.ijhydene.2007.02.018, URL https://www.sciencedirect.com/science/article/pii/S0360319907001176.

[42] C. McHardy, G. Luzi, C. Lindenberger, J.R. Agudo, A. Delgado, C. Rauh, Numerical analysis of the effects of air on light distribution in a bubble column photobioreactor, Algal Res. 31 (2018) 311–325, http://dx.doi.org/10.1016/j.algal.2018.02.016, URL https://www.sciencedirect.com/science/article/pii/S2211926417309426.

[43] J. Akach, J. Kabuba, A. Ochieng, Simulation of the Light Distribution in a Solar Photocatalytic Bubble Column Reactor Using the Monte Carlo Method, Ind. Eng. Chem. Res. 59 (40) (2020) 17708–17719, http://dx.doi.org/10.1021/acs.iecr.0c02124, Publisher: American Chemical Society.

[44] L. Pilon, R. Viskanta, Radiation Characteristics of Glass Containing Gas Bubbles, J. Am. Ceram. Soc. 86 (8) (2003) 1313–1320, http://dx.doi.org/10.1111/j.1151-2916.2003.tb03468.x, _eprint: https://onlinelibrary.wiley.com/doi/pdf/10.1111/j.1151-2916.2003.tb03468.x. URL https://onlinelibrary.wiley.com/doi/abs/10.1111/j.1151-2916.2003.tb03468.x.

[45] J. Randrianalisoa, D. Baillis, L. Pilon, Modeling radiation characteristics of semitransparent media containing bubbles or particles, J. Opt. Soc. Amer. A 23 (7) (2006) 1645–1656, http://dx.doi.org/10.1364/JOSAA.23.001645, URL https://opg.optica.org/josaa/abstract.cfm?uri=josaa-23-7-1645. Publisher: Optica Publishing Group.

[46] L.A. Dombrovskii, The Propagation of Infrared Radiation in a Semitransparent Liquid Containing Gas Bubbles, High Temp. 42 (1) (2004) 146–153, http://dx.doi.org/10.1023/B:HITE.0000020103.82678.13.

[47] W. Jiang, W. Levasseur, J. Casalinho, T. Martin, F. Puel, P. Perré, V. Pozzobon, Shear stress computation in a millimeter thin flat panel photobioreactor: Numerical design validated by experiments, Biotechnol. Appl. Biochem. 68 (1) (2021) 60–70, http://dx.doi.org/10.1002/bab.1894, _eprint: https://iubmb.onlinelibrary.wiley.com/doi/pdf/10.1002/bab.1894. URL https://iubmb.onlinelibrary.wiley.com/doi/abs/10.1002/bab.1894.

[48] X. Zhang, Z. Jiang, L. Chen, A. Chou, H. Yan, Y.Y. Zuo, X. Zhang, Influence of cell properties on rheological characterization of microalgae suspensions, Bioresour. Technol. 139 (2013) 209–213, http://dx.doi.org/10.1016/j.biortech.2013.03.195, URL https://www.sciencedirect.com/science/article/pii/S0960852413005993.

[49] A. Cartellier, M. Andreotti, P. Sechet, Induced agitation in homogeneous bubbly flows at moderate particle Reynolds number, Phys. Rev. E 80 (6) (2009) 065301, http://dx.doi.org/10.1103/PhysRevE.80.065301, URL https://link.aps.org/doi/10.1103/PhysRevE.80.065301. Publisher: American Physical Society.

[50] J.-C. Shyu, C.-W. Chang, P.-H. Chen, A Simplified Correlation for Bubble Volume Estimation, Can. J. Chem. Eng. 84 (2) (2006) 183–188, http://dx.doi.org/10.1002/cjce.5450840205, _eprint: https://onlinelibrary.wiley.com/doi/pdf/10.1002/cjce.5450840205. URL https://onlinelibrary.wiley.com/doi/abs/10.1002/cjce.5450840205.

[51] H. Jasak, A. Jemcov, Z. Tukovic, OpenFOAM: A c++ library for complex physics simulations, in: International Workshop on Coupled Methods in Numerical Dynamics, vol. 1000, Dubrovnik, Croatia), 2007, pp. 1–20.

[52] L.G. Henyey, J.L. Greenstein, Diffuse radiation in the Galaxy., Astrophys. J. 93 (1941) 70–83, http://dx.doi.org/10.1086/144246, URL https://ui.adsabs.harvard.edu/abs/1941ApJ....93...70H. Publisher: IOP ADS Bibcode: 1941ApJ....93...70H.

[53] J.R. Howell, M.P. Menguc, K. Daun, R. Siegel, Thermal Radiation Heat Transfer, Seventh ed., CRC Press, Boca Raton, 2020.

[54] B. Barankova, D. Lazar, J. Naus, A. Solovchenko, O. Gorelova, O. Baulina, G. Huber, L. Nedbal, Light absorption and scattering by high light-tolerant, fast-growing Chlorella vulgaris IPPAS C-1 cells, Algal Res. 49 (2020) 101881, http://dx.doi.org/10.1016/j.algal.2020.101881, URL https://www.sciencedirect.com/science/article/pii/S2211926419310963.

[55] P.E. Ciddor, Refractive index of air: new equations for the visible and near infrared, Appl. Opt. 35 (9) (1996) 1566–1573, http://dx.doi.org/10.1364/AO.35.001566, URL https://opg.optica.org/ao/abstract.cfm?uri=ao-35-9-1566. Publisher: Optica Publishing Group.

[56] G.M. Hale, M.R. Querry, Optical Constants of Water in the 200-nm to 200-âμm Wavelength Region, Appl. Opt. 12 (3) (1973) 555–563, http://dx.doi.org/10.1364/AO.12.000555, URL https://opg.optica.org/ao/abstract.cfm?uri=ao-12-3-555. Publisher: Optica Publishing Group.

[57] X. Zhang, J. Qiu, X. Li, J. Zhao, L. Liu, Complex refractive indices measurements of polymers in visible and near-infrared bands, Appl. Opt. 59 (8) (2020) 2337–2344, http://dx.doi.org/10.1364/AO.383831, URL https://opg.optica.org/ao/abstract.cfm?uri=ao-59-8-2337. Publisher: Optica Publishing Group.

[58] Y. Gong, J. Li, Y. Zhou, Y. Li, H.S. Chung, Y. Shi, J. Zhang, Genetic Learning Particle Swarm Optimization, IEEE Trans. Cybern. 46 (10) (2016) 2277–2290, http://dx.doi.org/10.1109/TCYB.2015.2475174.

[59] D. Molin, C. Marchioli, A. Soldati, Turbulence modulation and microbubble dynamics in vertical channel flow, Int. J. Multiph. Flow 42 (2012) 80–95, http://dx.doi.org/10.1016/j.ijmultiphaseflow.2012.01.010, URL https://www.sciencedirect.com/science/article/pii/S0301932212000201.